



## Unexpected strength–ductility response in an annealed, metastable, high-entropy alloy

S.S. Nene<sup>a</sup>, S. Sinha<sup>a</sup>, M. Frank<sup>a</sup>, K. Liu<sup>a</sup>, R.S. Mishra<sup>a,\*</sup>, B.A. McWilliams<sup>b</sup>, K.C. Cho<sup>b</sup>

<sup>a</sup> Center for Friction Stir Processing, Department of Materials Science and Engineering, University of North Texas, Denton, TX 76207 USA

<sup>b</sup> Weapons and Materials Research Directorate, U.S. Army Research Laboratory, Aberdeen Proving Grounds, MD 21005 USA

### ARTICLE INFO

#### Article history:

Received 5 July 2018

Received in revised form 4 September 2018

Accepted 10 September 2018

#### Keywords:

Annealing

Transformation-induced plasticity (TRIP)

High-entropy alloys (HEAs)

Precipitation

Work hardening

### ABSTRACT

The design of non-equiautomic high-entropy alloys (HEAs) opens huge compositional space to develop new materials with exceptional properties. Among them, HEAs with flexible microstructures showed an adaptive phase stability that enhanced the work hardening (WH) ability of the material drastically. With the same motive, here we present a new friction stir processed  $\text{Fe}_{39}\text{Mn}_{20}\text{Co}_{20}\text{Cr}_{15}\text{Si}_5\text{Al}_1$  HEA that demonstrated an unexpected strength–ductility response just upon annealing. The inter-competing precipitation and grain/twin formation events during low-temperature annealing resulted in an unexpected  $\text{f.c.c.}(\gamma) \rightarrow \text{h.c.p.}(\varepsilon)$  transformation. This unusual phase evolution triggered development of refined,  $\varepsilon$ -dominated microstructure coupled with a uniformly dispersed fine  $\gamma$  phase. The controlled  $\langle\text{c+a}\rangle$  slip and twinning in the  $\varepsilon$  phase along with the transformation of a refined  $\gamma$  matrix resulted in higher elongation of 52% with enhanced ultimate tensile strength of 1.12 GPa during deformation. Thus, the metastability-assisted design of  $\varepsilon$ -martensite-dominant HEAs by annealing opens a new path to obtain strong yet ductile alloys, which is otherwise not feasible in conventional steel/HEA designs.

© 2018 Elsevier Ltd. All rights reserved.

## 1. Introduction

The effort toward design of dual-phase high-entropy alloys (DP-HEAs) has been based on obtaining alloy compositions that have higher tensile strengths with greater elongations [1–4]. Conventional materials fail to overcome the conventional strength–ductility trade-off; hence, the concept of non-equiautomic addition of elements has attracted researchers in a very short time span [1–4]. Earlier work on equiautomic HEAs showed uncommon mechanical, wear and fatigue properties that were attributed mainly to the complex concentrated solid solutions formed by suppressing brittle intermetallic compounds [5–9]. Further development in this field has led to the development of dual-phase non-equiautomic DP-HEAs that displayed extraordinary work hardening because of the synergistic activation of dislocation-, transformation- and twinning-related mechanisms during deformation [1–4,10]. The overall HEA design strategies used till date have been based on tuning the stacking fault energy (SFE) of the alloys [1–10]. SFE is crucial in altering the stability of the  $\text{f.c.c.}(\gamma)$  matrix, which in turn governs microstructural engineering during

the thermo-mechanical processing of HEAs. A key additional benefit of non-equiautomic HEA design is related to opening huge compositional space (away from the center of the phase diagram) for developing new alloys. Our recent work of metastability-based design of a non-equiautomic  $\text{Fe}_{40}\text{Mn}_{20}\text{Co}_{20}\text{Cr}_{15}\text{Si}_5$  (termed as CS-HEA) resulted in responsive microstructural evolution upon friction stir processing (FSP, which we called “microstructural flexibility”) in an alloy that reversed strength–ductility relation, thereby overcoming the conventional strength–ductility trade-off [3]. We attributed this untraditional behavior of the CS-HEA to the kinetic phase stabilization upon FSP and the controlled transformation of the metastable  $\gamma$  matrix and twinning in the  $\text{h.c.p.}(\varepsilon)$  phase during subsequent tensile deformation [3,4]. Along with exceptional strength–ductility, we attained very good yield strength (YS) for CS-HEA. To increase the YS and work hardening ability of CS-HEA further by tuning the  $\gamma$  phase stability, we altered its composition with the minor addition of 1 at.% Al. Hence, the composition of the new HEA was selected as  $\text{Fe}_{39}\text{Mn}_{20}\text{Co}_{20}\text{Cr}_{15}\text{Si}_5\text{Al}_1$  (all at.%). For retaining microstructural flexibility upon processing in  $\text{Fe}_{39}\text{Mn}_{20}\text{Co}_{20}\text{Cr}_{15}\text{Si}_5\text{Al}_1$  (henceforth designated as Al-HEA), FSP was used for microstructural engineering in the present work, since FSP is a unique process wherein all processing parameters (strain, strain rate, time and temperature) can be controlled in synergy without changing the cross-section of the material [11].

\* Corresponding author.

E-mail address: [Rajiv.Mishra@unt.edu](mailto:Rajiv.Mishra@unt.edu) (R.S. Mishra).

**Table 1**  
Processing parameters selected for D-pass FSP processing.

Processing parameters	D-pass	
	Pass 1	Pass 2
Rotational rate (rpm)	350	150
Traverse speed (mm/min)	50.8	50.8
Plunge depth (mm)	3.65	3.65
Tilt angle (°)	2.0	2.0

In addition, the effect of precipitation on mechanical response was studied by annealing the friction stir processed Al-HEA.

## 2. Experimental

### 2.1. Material and processing

The Al-HEA was produced by vacuum arc-casting in a cold-copper crucible. The vacuum level achieved was approximately 300 μm, and the chamber was backfilled with argon to 1 atm prior to each melt, using pure metals with a nominal composition of Fe<sub>39</sub>Mn<sub>20</sub>Co<sub>20</sub>Cr<sub>15</sub>Si<sub>5</sub>Al<sub>1</sub> (at.%) and ingot dimensions of 300 × 100 × 6 mm<sup>3</sup>. Subsequently, these 6 mm thick sheets were FSP using a W-Re tool with the parameters shown in Table 1. Double pass (D-pass) processing essentially involves two overlapping FSP runs starting with a 350 rpm run followed by an overlapping run at 150 rpm. A Cu backing plate was used for effective heat dissipation, and Ar was blown near the specimen tool interface for avoiding oxygen pickup during processing. The processing tool had a shoulder diameter of 12 mm with a tapered pin. The root diameter, pin diameter and length of the tool were 7.5, 6, and 3.5 mm, respectively.

### 2.2. Annealing Treatment

Annealing treatment was carried out in a muffle furnace at 650, 750 and 850 °C. Mini tensile samples (details below) from D-pass conditions were packed in thin stainless steel foil and then kept in the furnace once the set temperature was attained. Stainless steel foil was used to avoid oxidation. The samples were taken out from the furnace after 5, 15 and 30 min each and quenched in water. The quenched specimens were then taken out from the foil and polished to remove any surface oxide layer that may have formed.

### 2.3. Microstructural characterization and tensile testing

Microstructures of the alloy in as-cast (coarse-grained) and as-FSP (grain-refined) conditions were analyzed by various methods. X-ray diffraction (XRD) measurements were performed using a RIGAKU X-ray machine equipped with Cu Kα radiation operated at 40 kV and 30 mA. Electron backscatter diffraction (EBSD) measurements were carried out by an FEI NOVA Nano scanning electron microscope (SEM) with a Hikari camera, and the data were analyzed using TSL OIM 8 software. The coarse grained HEA EBSD was carried out at a magnification of 600× with a step size of 0.8 μm and area of 273 × 218 μm<sup>2</sup>. As the grain size attained during FSP was significantly fine, EBSD scans were done at two magnifications, i.e. 2000× and 6000×. In order to capture enough number of grains during high-magnification scans (6000×), grain size and phase fractions were estimated at three different locations and the average values have been reported. The step size and the scan area used for all FSP + annealing conditions for 6000× scans were 0.08 μm and 25 × 20 μm<sup>2</sup>, respectively.

Rectangular, 1-mm thick, dog-bone-shaped mini-tensile specimens were machined using a computer numerical control machine from 1 mm below the surface within the nugget region of all

FSP specimens, whereas specimens for the as-cast condition were machined from the top surface of the as-cast ingot. Gage length and width of the tensile specimens were 5 and 1.25 mm, respectively. In each condition, three samples were tested at room temperature and an initial strain rate of 10<sup>-3</sup> s<sup>-1</sup> to confirm reproducibility of the results.

## 3. Results

### 3.1. Alloy design strategy and microstructural evolution in the as-cast and as-FSP Al-HEA

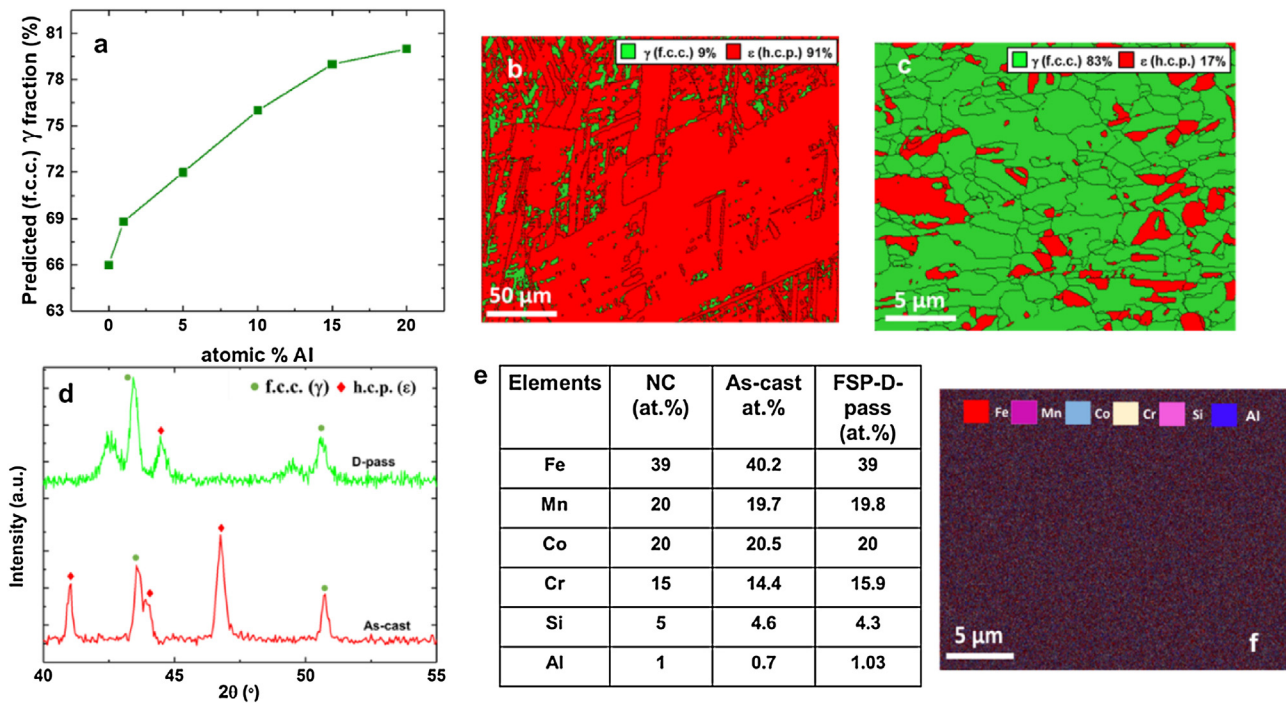
As discussed in Section 1, Al addition was intended to attain more sustained work hardening in the material during deformation by tuning γ phase stability. The effect of Al content on γ phase stability was determined using Thermo-Calc. Fig. 1a shows the outcome of the simulations and confirms that γ matrix becomes more stable with increase in Al content in Fe<sub>40-x</sub>Mn<sub>20</sub>Co<sub>20</sub>Cr<sub>15</sub>Si<sub>5</sub>Al<sub>x</sub> system. Our recent work [3] showed that increase in γ metastability is a key factor for having adaptive phase stabilization resulting in exceptional strength-ductility response in CS-HEA. Therefore, minor addition of 1 at.% Al was done resulting in the composition of Fe<sub>39</sub>Mn<sub>20</sub>Co<sub>20</sub>Cr<sub>15</sub>Si<sub>5</sub>Al<sub>1</sub>.

Fig. 1b-f depicts the microstructural evolution in the as-cast and friction stir processed Al-HEA. As expected, the as-cast specimen displayed dual-phase microstructure with 90% ε and 10% γ as shown in the EBSD phase map (Fig. 1b) which is also supported by the XRD pattern that showed distinct peaks for both phases (Fig. 1d). As reported in our recent work on CS-HEA [3], the D-pass (specimens processed with two overlapping passes of FSP at 350 and 150 rpm, respectively) specimen exhibited the best mechanical response and thus the same processing parameters were kept for FSP of Al-HEA.

Fig. 1c shows the γ phase dominant dual-phase microstructure for Al-HEA resulting from D-pass processing. FSP refined the microstructure of Al-HEA significantly and resulted in an average grain size of 0.79 ± 0.05 μm from the as-cast grain size of 120 ± 12 μm. The higher fraction of the γ phase in the D-pass specimen is a strong indication of decreased metastability of the γ matrix due to the minor addition of Al [12,13] upon FSP and supports the Thermo-Calc predictions in Fig. 1a. This decreased γ metastability indirectly suggests that Al addition decreased the tendency of adaptive phase stability with processing parameters in the material as was seen in CS-HEA [3]. Further, Fig. 1d and e confirms the retention of chemical homogeneity in the material upon FSP as well as in the as-cast condition, since the elemental distribution in both conditions appears very close to nominal composition (NC) of Al-HEA (Fig. 1e). All the values of elemental fractions reported in Fig. 1e are within ±1.5–5.2%.

### 3.2. Phase evolution upon annealing of the as-FSP Al-HEA

Fig. 2a shows the annealing cycle used in the study. The symbols 650-X, 750-X, and 850-X correspond to annealing at 650, 750 and 850 °C, respectively. Detailed steps for these annealing conditions are given in Table 2. XRD and EBSD analyses make it clear that ε and γ phase fractions changed substantially with annealing time irrespective of annealing temperature. However, unconventional phase evolution occurred for 650-X and 850-X conditions at 15 and 30 min, respectively. As per the evaluated phase diagram from Thermo-Calc (see Section 4) for Al-HEA, both 650 and 850 °C are sufficiently high temperatures to stabilize the γ phase with time. As a result, with increased annealing time for 650-X or 850-X conditions, the fraction of the γ phase should increase. On the contrary, the γ phase fraction decreased (Fig. 2b) for both



**Fig. 1.** Microstructural evolution in Al-HEA upon FSP. (a) Thermo-Calc (TCHEA2 database) predictions for  $\gamma$  phase fractions at room temperature as a function of Al content in  $\text{Fe}_{40-x}\text{Mn}_{20}\text{Co}_{20}\text{Cr}_{15}\text{Si}_5\text{Al}_x$  system, (b) as-cast microstructure, (c) EBSD phase maps for D-pass condition, (d) X-ray diffraction analysis for the as-cast and D-pass specimens, and (e and f) EDS elemental distribution with nominal composition and EDS X-ray map for the D-pass condition for Al-HEA. NC, nominal composition of Al-HEA; FSP, friction stir processing; EBSD, electron backscattered diffraction; EDS, energy dispersive spectroscopy.

annealing conditions at 15 and 30 min, respectively. This unexpected  $\gamma \rightarrow \epsilon$  transformation was further confirmed from XRD analysis wherein distinct peaks were obtained for the  $\epsilon$  phase (highlighted by dotted ellipse in Fig. 2c) for the 650-15, 650-30 and 850-30 specimens, indicating decrease in  $\gamma$  phase fraction for these conditions after annealing. Fig. 2d<sub>1</sub>–d<sub>4</sub> are EBSD phase maps for the 650-15, 650-30, 850-15 and 850-30 specimens and also display the  $\epsilon$  phase (red color) in the microstructure with different  $\epsilon$  morphology and distribution in each of them. This morphological and distributional variation in the  $\epsilon$  phase is expected to affect the mechanical response significantly during subsequent deformation [1–5].

Fig. 3a–i shows the precipitate evolution in Al-HEA upon different annealing conditions. Among them, Fig. 3a–c depicts the EBSD image quality (IQ) maps for the 650-5, 650-15 and 650-30 specimens, respectively. Controlled precipitation and grain growth are seen even after 30 min of annealing at 650 °C. Higher soaking temperature (850 °C) for 850-X annealing resulted in massive precipitation and grain growth (Fig. 3d–f). Fig. 3e shows the back scattered electron (BSE) image for the 850-15 specimen showing coarse grain structure with large Al-rich precipitates at the grain boundaries and having almost 97%  $\gamma$  phase as against the relatively refined martensite-dominated microstructure for the 850-30 specimen. Thus, high-temperature annealing showed nearly single-phase  $\gamma$  microstructure up to 15 min of annealing and an unusual  $\gamma \rightarrow \epsilon$  transformation occurred after that. This unusual phase evolution is associated with counteracting effects of the grain growth and precipitation events occurring at respective annealing time and temperatures.

The overall change in grain size and Al content in the matrix with annealing time (Fig. 3g and h) also supports the observation of more sluggishness in grain growth and precipitation for 650-X than for the 850-X-treated specimens. Detailed analysis of precipitates (Fig. 3i) by EDS-X-ray mapping shows the formation of Al-rich precipitates formed near the grain boundaries upon 15 min

of annealing. The precipitate size and morphology got changed with increase in soaking time as confirmed in BSE image for the 850-30 specimen (Fig. 3f). In short, the Al content decreased with annealing time (Fig. 3h) and the precipitate size increased with annealing temperature (Fig. 3a–f). The structural and morphological characterization and quantification of the precipitates is under investigation and would be reported in subsequent studies.

### 3.3. Tensile properties for the as-annealed Al-HEA

Fig. 4a and b displays the engineering stress–engineering strain curves for 650-X and 850-X annealing conditions, respectively. An almost 150 MPa increase in ultimate tensile strength (UTS) with a 15% increase in total elongation for the 650-X-treated specimens was apparent. However, 850-X annealing showed conventional reduction in the UTS values with increasing elongation compared to the D-pass condition (green curve in Fig. 4b). YS for the 650-X-annealed specimens was similar to that of the D-pass condition, whereas the 850-X-annealed specimens show almost 200 MPa drop in YS. Among all processing and annealing conditions, 650-15 demonstrated an exceptional combination of UTS (1.12 GPa), YS (610 MPa) and total elongation (52%). Also, within the 650-X-treated specimens, 15 and 30 min of annealing (dark golden and blue curves in Fig. 4a) showed increased UTS values with almost similar/more elongation compared to 5 min annealing specimen. However, the conventional trend of drop in UTS with elongation was consistent for the 850-X annealing specimens (Fig. 4b) as a function of annealing time.

Fig. 4c and d presents true stress–true strain curves plotted along with the work hardening (WH) curves for 650-X and 850-X annealing conditions, respectively. Among all, 650-30 showed the highest true tensile strength of 1.63 GPa, with a uniform elongation of almost 43% and, hence, undergoes very sustained WH over a broader stress and strain range. However, as suggested earlier, upon annealing, the 850-X-annealed specimens

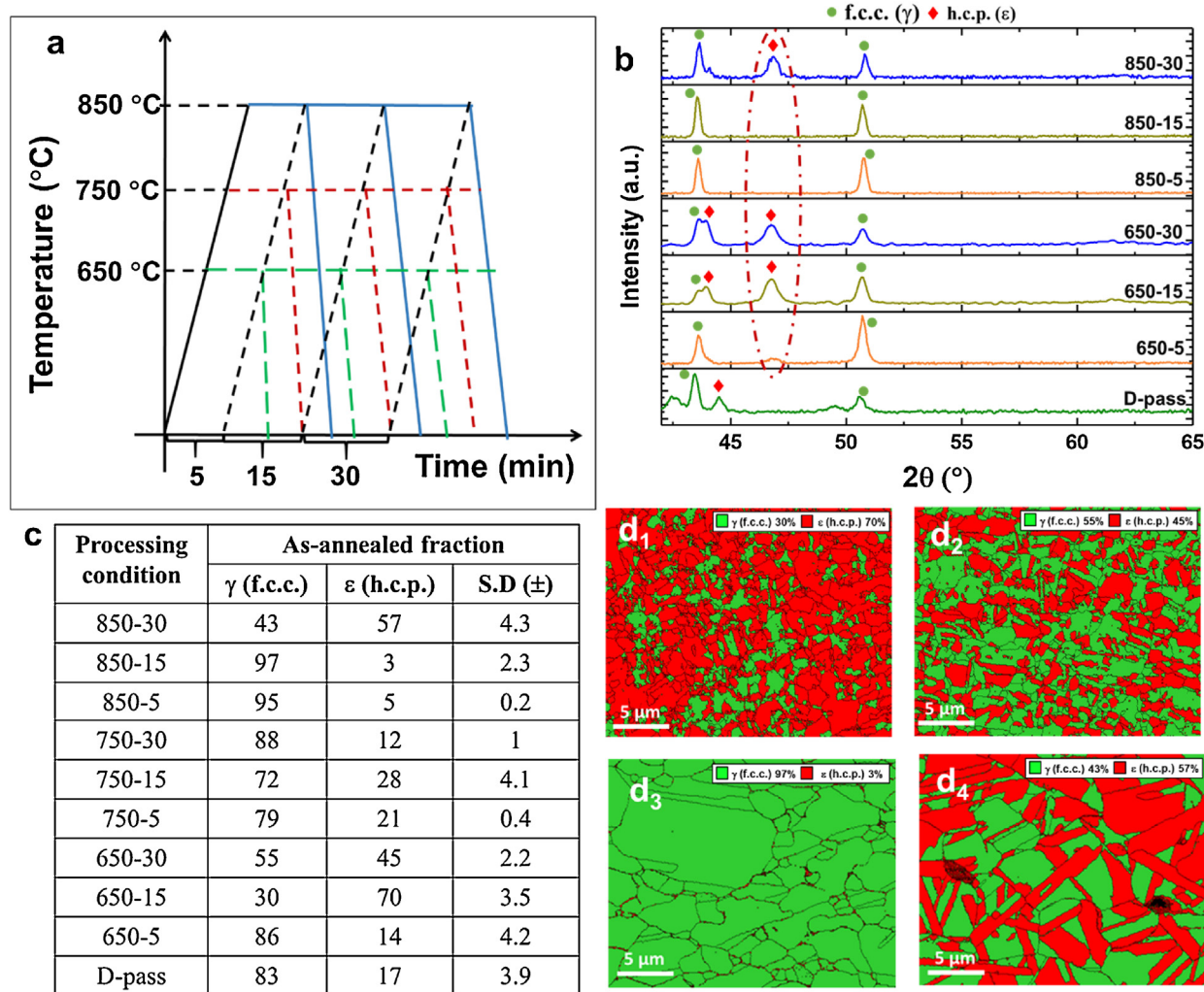


**Fig. 2.** Microstructural evolution upon annealing. (a) Annealing treatment cycle used in the present work. (b) XRD patterns for all annealing conditions compared with the D-pass condition. (c) A summary of phase fractions obtained in the Al-HEA for all annealing conditions, and EBSD phase maps for the (d<sub>1</sub>) 650-15, (d<sub>2</sub>) 650-30, (d<sub>3</sub>) 850-15 and (d<sub>4</sub>) 850-30 specimens (EBSD, electron backscattered diffraction; S.D., standard deviation).

**Table 2**  
Annealing treatments used in the present work.

Condition	Steps
650-X	D-pass specimen soaked at 650 °C for X min followed by quenching in water
750-X	D-pass specimen soaked at 750 °C for X min followed by quenching in water
850-X	D-pass specimen soaked at 850 °C for X min followed by quenching in water

confirmed an overall drop in true tensile properties. Irrespective of the processing condition, an abrupt change in the slope of the WH curve appeared at specific stress and strain values. This change in slope is associated with the transition in deformation mechanisms from dislocation-dominated to multiple mechanism-dominated [3,4,14–16]. Further, this change in slope divides the conventional stage III WH into two distinct sub-stages, namely (i) dislocation-dominated and (ii) transformation-dominated (sustained WH regime) as marked with the red lines for the 650-15 specimen in Fig. 4c. The change in slope for this specimen occurs at the WH rate of 2983 MPa, which corresponds to a true stress of 924 MPa (engineering stress of ~840 MPa) at ~10% elongation.

As transformation-induced plasticity (TRIP) is the primary deformation accommodation mechanism other than dislocations

in metastable HEAs [1–4], the onset stress value of 924 MPa (corresponding engineering stress of ~840 MPa) for transformation essentially determines the stress required to initiate  $\gamma \rightarrow \epsilon$  transformation during deformation in the 650-15 specimen and hence can be termed as TRIP stress. Similar analysis for other processing conditions also suggested that, depending on grain sizes and prior  $\epsilon$  phase fractions (i.e., annealing conditions), this value of stress changed significantly. Further, the conventional trend of decrease in UTS and YS with increase in ductility as a function of annealing time was reversed in the present work and an unexpected strength–ductility response was obtained for low-temperature annealed (with notable YS) specimens. This symbiotic mechanical response is associated mainly with the unpredicted phase evolution that occurred in the material at those annealing conditions and is discussed in subsequent sections.

## 4. Discussion

### 4.1. Unpredicted $\gamma \rightarrow \epsilon$ phase evolution upon annealing

Fig. 5a–e highlights the unusual  $\gamma \rightarrow \epsilon$  transformation that occurred in Al-HEA in the form of a flowchart. According to Thermo-Calc prediction (Fig. 5f), 650 °C belongs to the single-phase  $\gamma$  phase field and thus holding at such a temperature

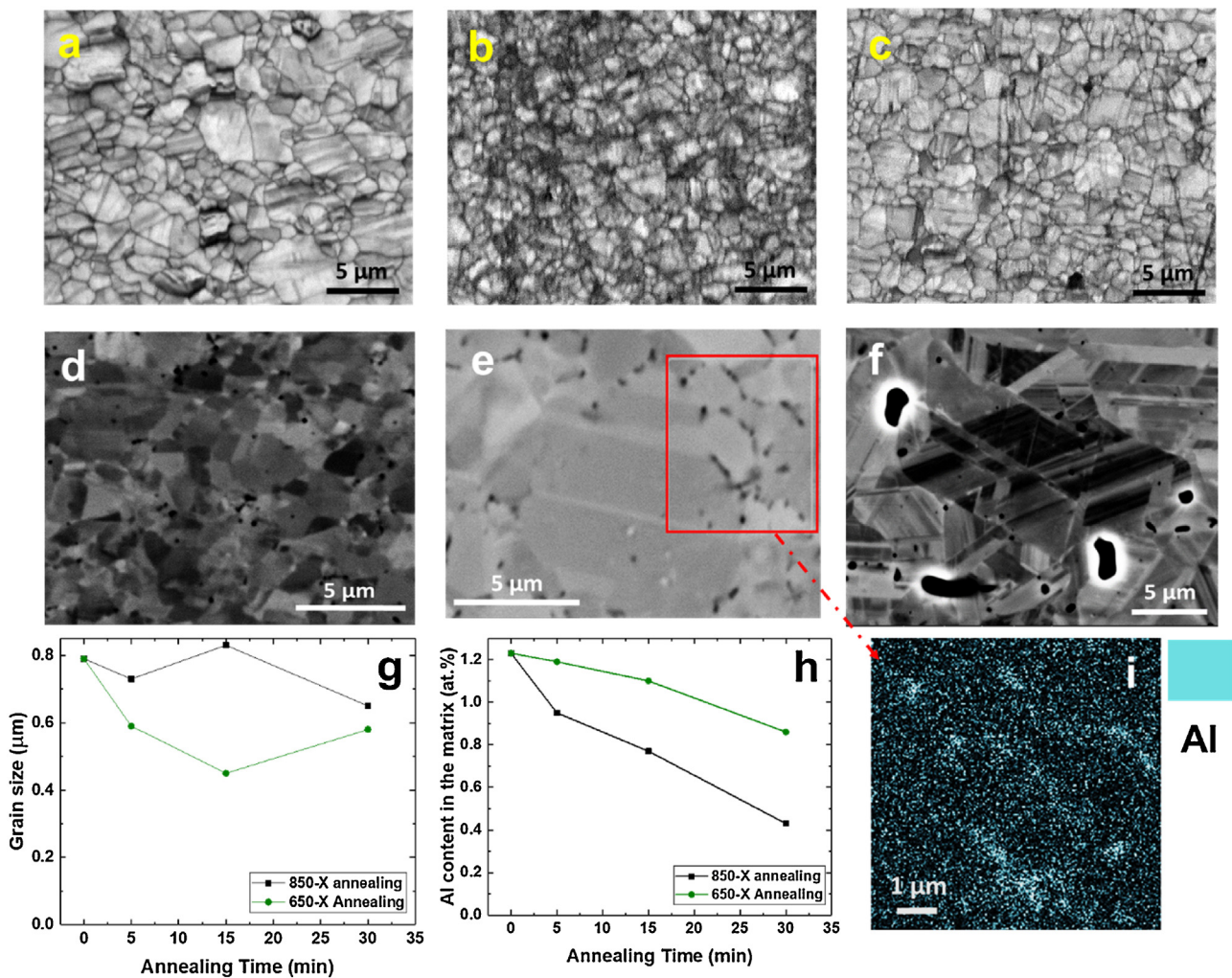


**Fig. 3.** Precipitate and grain size characterization. EBSD image quality (IQ) maps for the (a) 650-5, (b) 650-15 and (c) 650-30 specimens. Backscattered electron images for the (d) 850-5 (e) 850-15 and (f) 850-30 specimens. (g) Grain size variation with annealing time, and (h) variation of Al content in matrix with annealing time and (i) EDS X-ray map for Al-rich precipitates.

for longer times should produce higher fractions of  $\gamma$  in the microstructure. However, the exact opposite trend occurred in the present work, wherein a higher fraction of  $\varepsilon$  was obtained for both 15 and 30 min annealing at 650 °C (more red color in Fig. 5d and e and for 30 min at 850 °C (Fig. 5g). As per the phase diagram and thermodynamic considerations from Thermo-Calc database (Figs. 1a and 5f), Al addition in CS-HEA reduced metastability of the  $\gamma$  matrix [13]. However, if the Al is taken out from the solid solution in the form of second phase or precipitate, the resultant matrix will again become highly metastable, since it will approach the extremely metastable CS-HEA composition [3]. Thus, understanding the consequence of Al depletion in the matrix on  $\varepsilon$  phase formation is important, since increasing metastability essentially promotes faster martensite formation [1–4].

Also, since annealing accompanies grain boundary (GB) movements and ultimately affects the GB area attained for a given soaking time, grain growth events affect  $\gamma \rightarrow \varepsilon$  phase transformation [17–22]. Moreover, low SFE alloys like metastable HEAs have stable stacking fault packets in the lattice and also act as nucleation sites for annealing twins, which upon long enough holding time can grow to full grains [17–22]. Hence, unlike conventional materials, the synergistic occurrence of these phenomena in metastable HEAs governs the resultant  $\gamma$  matrix stability upon annealing. The brief

hypothesis about the unusual phase evolution in present work is explained with the schematic in Fig. 6.

To predict the overall effect of the annealing-assisted phenomenon on  $\gamma \rightarrow \varepsilon$  transformation, a schematic in Fig. 6 presents the microstructural evolution in the 650-15 and 850-30 specimens at the respective holding temperatures and after quenching. Fig. 6a<sub>1</sub> and a<sub>2</sub> suggests that 850 °C being a higher temperature, diffusion of Al would be faster and hence the result would be massive precipitation of the second phase during the soaking period (Fig. 6a<sub>2</sub>), thereby destabilizing the  $\gamma$  matrix more. However, this phenomenon is counteracted by rapid grain growth at such a high temperature (Fig. 6a<sub>2</sub>), which reduced nucleation sites for  $\varepsilon$  formation. As confirmed from Fig. 3e and f, there appeared substantial fractions of precipitates in the 850-X-treated specimens upon quenching with increase in average grain size (Fig. 3g). Moreover, notable decrease in the Al content in the matrix which also supports the rapid diffusion of Al to Al-rich particles (Fig. 3h) during annealing for longer times. Meanwhile, higher annealing temperature triggers rapid reorientations and causes localized twinning activity in coarser grains [21–25] (Fig. 6a<sub>1</sub>). Therefore, increase in matrix metastability due to massive precipitation coupled with excess twinning activity in coarser grains resulted in higher  $\varepsilon$  formation in the 850-30 specimen (Fig. 6a<sub>2</sub>) upon quenching. However, as confirmed from Fig. 2c and d<sub>3</sub>,

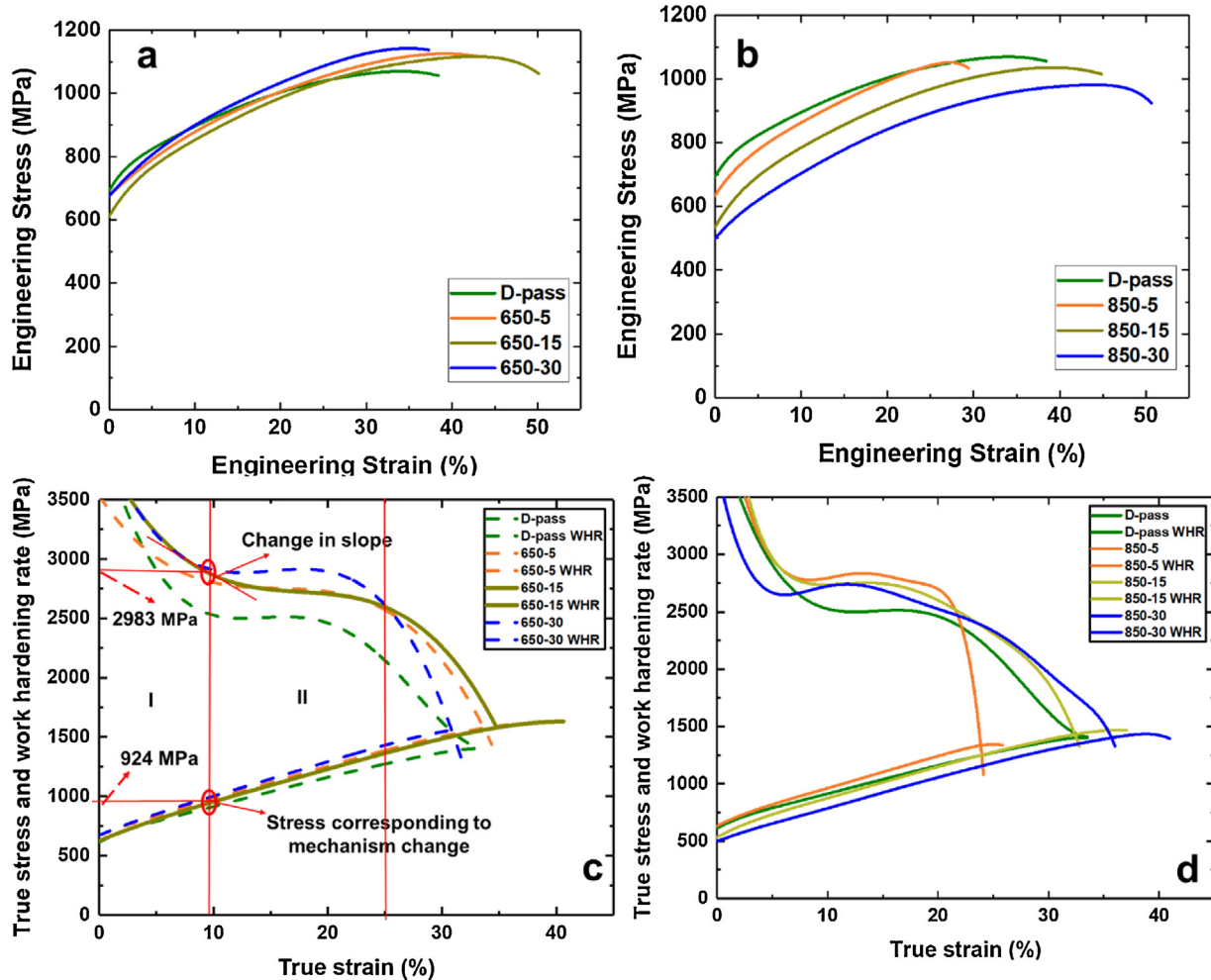


**Fig. 4.** Tensile properties of Al-HEA. (a) Engineering stress–engineering strain curves for the specimens annealed at 650 °C (650-X annealing), (b) engineering stress–engineering strain curves for specimens annealed at 850 °C (850-X annealing), (c) true stress–true strain and WH curves for specimens annealed at 650 °C (650-X annealing) and (d) true stress–true strain and WH curves for specimens annealed at 850 °C (850-X annealing).

850-15 showed  $\gamma$ -dominated microstructure as against the 850-30 specimen. This can be explained as follows: 15 min of soaking at 850 °C resulted in reduced precipitation and grain/twin formation kinetics (Fig. 3g and h) than 30 min of soaking owing to lesser time available for atomic movements and redistribution. As a result, metastability of the  $\gamma$  matrix got lowered due to higher Al dissolved in the matrix (Fig. 3h). Moreover, twinning activity also got suppressed (Fig. 2d<sub>3</sub>) due to shorter time available for reorientations and hence reduced the nucleation sites for  $\varepsilon$  formation upon quenching. Thus, increased  $\gamma$  stability and sluggish twin formation makes the  $\varepsilon$  formation difficult and give rise to  $\gamma$ -dominant microstructure after quenching in the 850-15 specimen.

In the case of 650-X treatment, 650 °C being lower temperature, Al diffusion becomes sluggish (as shown by the marginal variation in Al content in matrix in Fig. 3h), with a notable decrease in grain growth tendency (Fig. 3g). This limited grain growth suggests that low-temperature annealing retains more GB area with a controlled precipitation event (as fine precipitates were seen for the 650-X-treated specimens even for longer soaking times in Fig. 3b and c). This controlled precipitation makes the fine-grained  $\gamma$  matrix more metastable (Fig. 6a<sub>3</sub>) and thereby facilitates  $\varepsilon$  plate formation [22] during quenching (Fig. 6a<sub>3</sub> and a<sub>4</sub>). Therefore, a higher GB area combined with controlled precipitation would have enabled a higher  $\varepsilon$  phase fraction in the 650-15 specimen. This unexpected

$\gamma \rightarrow \varepsilon$  transformation was notably lower at 750 °C which suggests that both precipitation and grain growth/twin activities go hand-in-hand and hence maintain  $\gamma$  phase stability with annealing time for the 750-X-treated specimens. In summary, the synergistic effect of precipitation, grain growth and twinning with annealing temperature and time resulted in responsive phase evolution and hence provided annealing-assisted microstructural flexibility to the Al-HEA. The effect of this unconventional phase formation on the mechanical response is discussed in the subsequent sections.

#### 4.2. Unexpected strength–ductility response in annealed Al-HEA

Fig. 7a shows the WH plot for 650-X and 850-X annealing conditions that depicted not only unexpected phase evolution, but also exceptional stress–strain response (Fig. 4c–d). Detailed characteristics of deformation-related changes in those microstructures are presented in Fig. 7a–g. Fig. 7d and g has three corresponding micrographs that capture phase distribution, orientation distribution and geometrically-necessary dislocation density (GND) distribution for these annealing specimens after tensile deformation. As mentioned in Section 4.1, sustained WH over a broader strain regime provided Al-HEA with very high strength and ductility. However, the most interesting observation is the occurrence of constant WH over

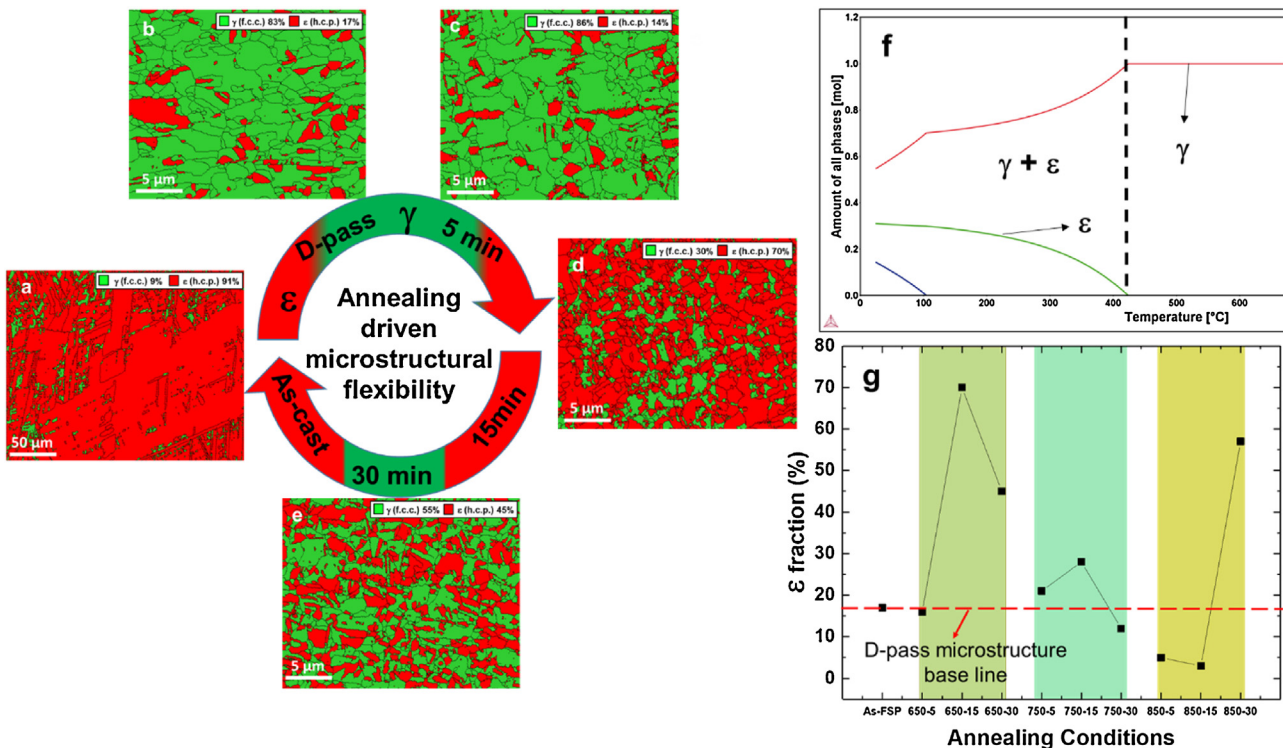


**Fig. 5.** Unconventional phase evolution during annealing. (a–e) Flowchart showing annealing-driven microstructural flexibility for the 650-X-annealed specimens, (f) thermodynamic phase predictions using Thermo-Calc for Al-HEA (TCHEA2 database was used) and (g) variation in  $\epsilon$  phase fraction with annealing conditions.

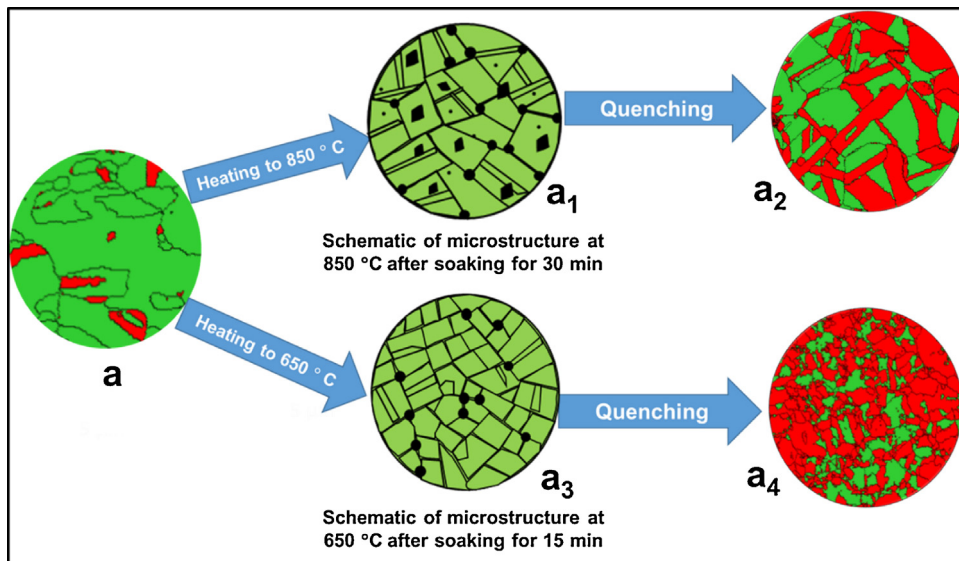


**Fig. 6.** Schematic showing  $\gamma \rightarrow \epsilon$  transformation in the (a<sub>1</sub>–a<sub>2</sub>) 850-30 and (a<sub>3</sub>–a<sub>4</sub>) 650-15 specimens.

almost 15% strain in  $\epsilon$ -dominated the 650-15 and 850-30 specimens (solid green and dotted blue curves in Fig. 7a).

The  $\epsilon$  (h.c.p.) phase is well known to have fewer slip systems available for room temperature deformation than the  $\gamma$  phase and hence its dominance would make the alloy harder and less ductile [1–4,26,27]. This argument was conquered by this work wherein a very strong  $\epsilon$  phase that can accommodate very significant amounts of strain during extensive loading was attained. Along with  $\gamma \rightarrow \epsilon$  transformation during deformation in both of these specimens (Fig. 7b and 7c), (c+a) slip (dislocation density  $\sim 5.1 \times 10^{15} \text{ m}^{-2}$ ) and twinning in  $\epsilon$  phase (Fig. 7c, d<sub>2</sub> and d<sub>1</sub>) made the material extremely damage-tolerant via dynamic Hall-Petch strengthening.

Uniform strain partitioning among these phases is also well known to help in improving ductility. GND measurements showed higher dislocation density values in  $\epsilon$  phase ( $\langle c+a \rangle$  dislocation density in  $\epsilon$  phase:  $5 \times 10^{15} \text{ m}^{-2}$ ) than in  $\gamma$  phase ( $1/2 \langle 110 \rangle$  dislocation density:  $2 \times 10^{15} \text{ m}^{-2}$ ) for the 650-15 and 850-30 specimens, respectively (GND distribution map, Fig. 7d<sub>3</sub> and g<sub>3</sub>). This dictates the active involvement of  $\epsilon$  phase in plastic deformation [1–4,28]. Higher dislocation accommodation in harder  $\epsilon$  phase also supports the fact that the transformed  $\epsilon$  phase is more ductile and damage tolerant.

According to earlier work on the TRIP-assisted alloys [1–5,10,29], a higher fraction of a very fine  $\epsilon$  phase within the  $\gamma$ -dominated matrix was reported to be desirable for attaining

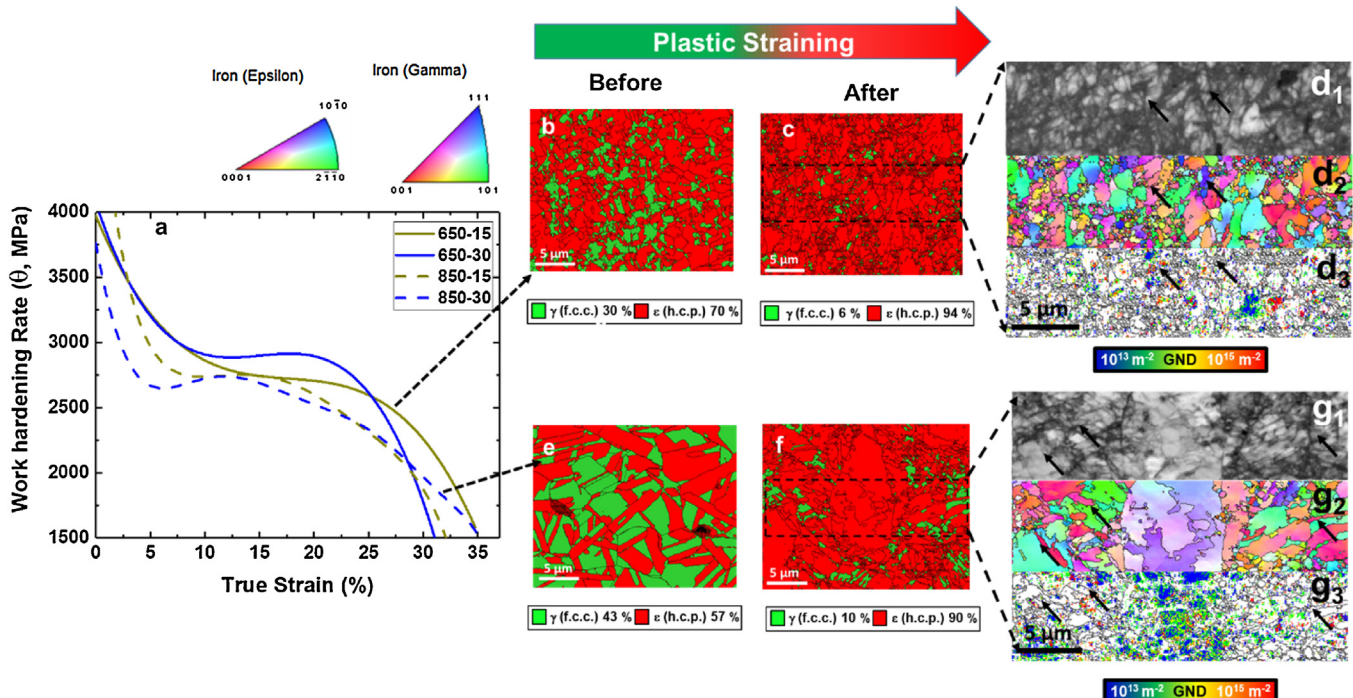


**Fig. 7.** Deformation mechanisms in Al-HEA. (a) WH rate ( $\theta$ ) vs plastic strain for selected annealing conditions. EBSD phase map for the 650-15 specimen (b) before and (c) after tensile deformation, EBSD maps depicting (d<sub>1</sub>: IQ; d<sub>2</sub>: IPF; d<sub>3</sub>: GND) for the 650-15 condition after tensile deformation, EBSD phase map for the 850-30 specimen (e) before and (f) after tensile deformation and EBSD maps depicting (g<sub>1</sub>: IQ; g<sub>2</sub>: IPF; g<sub>3</sub>: GND) for the 850-30 condition after tensile deformation. EBSD, electron backscattered diffraction; IPF, inverse pole figure; GND, geometrically necessary dislocations.

good strain hardening. However, the unusual  $\gamma \rightarrow \varepsilon$  transformation that occurred in the present work during annealing helped to produce a very fine-grained,  $\varepsilon$ -dominated dual-phase microstructure. Uniform distribution of a refined  $\gamma$  phase within the harder yet deformable  $\varepsilon$  phase triggered higher back stresses [1–4] on  $\gamma$  grains and thus resulted in a very controlled TRIP effect for Al-HEA in the 650-15 condition. This controlled TRIP effect further helped in attaining higher yet sustained WH resulting in an unexpected strength–ductility combination. In short, annealing-driven microstructural flexibility sets up a new milestone in non-equiautomic HEA design. As  $\gamma$  and  $\varepsilon$  phases are also crucial in governing other factors such as texture evolution, magnetic properties and reversible straining ability, this alloy design strategy opens possibilities for obtaining multi-functionality in HEA while maintaining its high strength and ductility.

Fig. 8 compares the strength–ductility index ((true UTS-YS)  $\times$  uniform elongation) of Al-HEA in various processing conditions with the strength–ductility index (SDI) values for TRIP HEAs and advanced TRIP steels reported to date [1–4,10,29–33]. Among all, Al-HEA in the 650-15 condition (marked in red shaded circle in Fig. 8) showed the highest SDI value (425 MPa) at reasonably high UTS value of 1.12 GPa, in spite of having a very high  $\varepsilon$  fraction ( $\sim 70\%$ ) prior to deformation. Earlier work on TRIP HEA reported a very high SDI value of  $\sim 450$  MPa, but at UTS less than 900 MPa and with  $\sim 32\%$   $\varepsilon$  phase fraction prior to deformation [1,10].

Our recent work on TRIP HEAs resulted in an exceptional increase in UTS and YS of the alloy with DP-5Si-HEA [4] and CS-HEA [3] (gray rightward half-filled triangle and sky blue half-filled diamond in Fig. 8) but with limited strain hardening ability. This drawback was overcome with the design of the Al-HEA, which showed almost 200 MPa higher SDI value with almost similar UTS as that of the CS-HEA [3]. Moreover, Al-HEA outperformed recently designed TRIP steels [30–33] in terms of SDI values, thereby opening a new compositional space to explore. As a result,

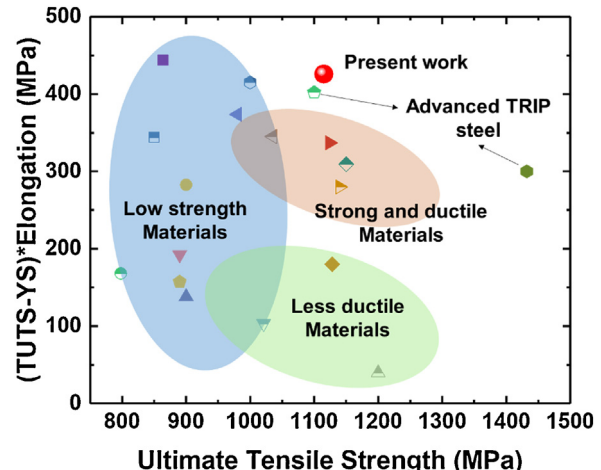


**Fig. 8.** Strength–ductility index values of Al-HEA compared with TRIP-assisted HEAs to date [1–4,10,29]. This includes DP-HEA [1,10], DP-i-HEA [2,29], Si-containing TRIP HEAs [4,5], advanced TRIP steels [30–33]. TRIP, transformation-induced plasticity.

this microstructural flexibility (processing- or annealing-based)-focused alloy design provides a more promising path for attaining unconventional mechanical properties, which is otherwise difficult to achieve in conventional steel design.

## 5. Conclusions

In summary, annealing of friction stir processed Al-HEA shows annealing triggered microstructural flexibility in the material through the self-tuning of matrix metastability via synergistic precipitation and grain growth events. Low-temperature annealing showed unconventional phase and grain evolution ( $\varepsilon$ -dominated) and an unexpected strength–ductility response. The ability of the  $\varepsilon$

phase to undergo uniform strain partitioning with the  $\gamma$  phase via  $(c+a)$  slip and twinning triggered sustained WH during deformation, thereby exhibited a very high SDI value of 425 MPa for Al-HEA at a higher UTS of 1.12 GPa. Thus, designing flexible microstructures provides a new path to obtain high-strength materials with exceptional ductility.

## Author contributions

S.S.N., S.S., M.F., K.L., R.S.M., R.E.B. and K.C.C. designed the research; S.S.N., S.S., M.F. and K.L. processed and characterized the alloy; S.S.N., S.S., M.F., K.L. and R.S.M. analyzed the results; S.S.N. and R.S.M. drafted the manuscript. All authors discussed the results and contributed to the final manuscript.

## Data availability statement

The raw/processed data required to reproduce these findings cannot be shared at this time as the data also forms part of an ongoing study.

## Conflicts of interest

The authors declare no competing financial and non-financial interests.

## Acknowledgments

The work was performed under a cooperative agreement between the Army Research Laboratory and the University of North Texas (W911NF-13-2-0018). The authors are thankful to the Materials Research Facility for providing access to the microscopy facilities at the University of North Texas. The authors also acknowledge help from J. Jacobson, S. Zellner and J. Reeder in EBSD and tensile specimens preparation.

## References

- [1] Z. Li, K.G. Pradeep, Y. Deng, D. Raabe, C.C. Tasan, Metastable high-entropy dual-phase alloys overcome the strength–ductility trade-off, *Nature* 534 (2016) 227–230.
- [2] Z. Li, C.C. Tasan, H. Springer, B. Gault, D. Raabe, Interstitial atoms enable joint twinning and transformation induced plasticity in strong and ductile high-entropy alloys, *Sci. Rep.* 7 (2017) 40704.
- [3] S.S. Nene, M. Frank, K. Liu, S. Sinha, R.S. Mishra, B. McWilliams, K.C. Cho, Reversed strength–ductility relationship in microstructurally flexible high entropy alloy, *Scripta Mater.* 154 (2018) 163–167.
- [4] S.S. Nene, M. Frank, K. Liu, R.S. Mishra, B. McWilliams, K.C. Cho, Extremely high strength and work hardening ability in a metastable high entropy alloy, *Sci. Rep.* 8 (2018) 9920.
- [5] J. Yeh, S.K. Chen, S. Lin, J.Y. Gan, T.S. Chin, T.T. Shun, C.H. Tsau, S.Y. Chang, Nanostructured high entropy alloys with multiple component elements: novel alloy design concepts and outcomes, *Adv. Eng. Mater.* 6 (2004) 299–303.
- [6] L.J. Santodonato, Y. Zhang, M. Feygenson, C.M. Parish, M.C. Gao, R.J.K. Weber, J.C. Neufeind, Z. Tang, P.K. Liaw, Deviation from high-entropy configurations in the atomic distributions of a multi-principal-element alloy, *Nature Commun.* 6 (2015) 5964.
- [7] D.B. Miracle, O.N. Senkov, A critical review of high entropy alloys and related concepts, *Acta Mater.* 122 (2017) 448–511.
- [8] M.A. Hemphill, T. Yuan, G.Y. Wang, J.W. Yeh, C.W. Tsai, A. Chuang, P.K. Liaw, Fatigue behavior of Al<sub>0.5</sub>CoCrFeNi high entropy alloys, *Acta Mater.* 60 (2012) 5723–5734.
- [9] Y. Shi, B. Yang, X. Xie, J. Brecht, K.A. Dahmen, P.K. Liaw, Corrosion of Al<sub>x</sub>CoCrFeNi high-entropy alloys: Al-content and potential scan-rate dependent pitting behavior, *Corr. Sci.* 119 (2017) 33–45.
- [10] S.S. Nene, K. Liu, M. Frank, R.S. Mishra, R.E. Brennan, K. Cho, Z. Li, D. Raabe, Enhanced strength and ductility in friction stir processed engineered high entropy alloy, *Sci. Rep.* 7 (2017) 16167.
- [11] S. Palanivel, A. Arora, K.J. Doherty, R.S. Mishra, A framework for shear driven dissolution of thermally stable particles during friction stir welding and processing, *Mater. Sci. Eng. A* 678 (2016) 308–314.
- [12] R. Xiong, H. Peng, H. Si, W. Zhang, Y. Wen, Thermodynamic calculation of stacking fault energy of the Fe–Mn–Si–C high manganese steels, *Mater. Sci. Eng. A* 598 (2014) 376–386.
- [13] D.T. Pierce, J.A. Jimenez, J. Bentley, D. Raabe, C. Oskay, J.E. Wittig, The influence of manganese content on the stacking fault and austenite/ $\epsilon$ -martensite interfacial energies in Fe–Mn–(Al–Si) steels investigated by experiment and theory, *Acta Mater.* 68 (2014) 238–253.
- [14] B.C. De Cooman, Y. Estrin, S.K. Kim, Twinning induced plasticity steels, *Acta Mater.* 142 (2018) 283–362.
- [15] Z.C. Cordero, B.E. Knight, C.A. Schuh, Six decades of the Hall-Petch effect—a survey of grain size strengthening studies on pure metals, *Int. Mater. Rev.* 61 (2015) 495–512.
- [16] R. Song, D. Ponge, D. Raabe, Improvement of the work hardening rate of ultrafine grained steels through second phase particles, *Scr. Mater.* 52 (2005) 1075–1080.
- [17] E.I. Galindo-Navia, P.E.J. Rivera-Díaz-del-Castillo, Understanding martensite and twin formation in austenitic steels: A model describing TRIP and TWIP effects, *Acta Mater.* 128 (2017) 120–134.
- [18] L.Y. Pustov, V.V. Tcherdyntsev, S.D. Kaloshkin, E.I. Estrin, E.V. Shelekhov, A.I. Laptev, D.V. Gunderov, Face-centered cubic phase stability and martensitic transformation under deformation in Fe–Ni and Fe–Mn alloys nanostructured by mechanical alloying and high-pressure torsion, *Mater. Sci. Eng. A* 481 (2008) 732–736.
- [19] S.T. Pisarik, D.C. Van Aken, Thermodynamic driving force of the  $\gamma \rightarrow \epsilon$  transformation and resulting  $M_s$  temperature in high-Mn steels, *Metall. Mater. Trans. A* 47 (2016) 1009–1018.
- [20] F. Trichter, A study  $\gamma \rightarrow \epsilon$  phase transformation in Fe–Mn alloys induced by high pressure and plastic deformation, *Scripta Metall.* 12 (1978) 431–434.
- [21] S. Martin, C. Ullrich, D. Rafaja, Deformation of austenitic CrMnNi TRIP/TWIP Steels: nature and role of the  $\epsilon$  martensite, *Mater. Today Proc.* 2 (2015) 643–646.
- [22] M. Wang, Z. Li, D. Raabe, In-situ SEM observation of phase transformation and twinning mechanisms in an interstitial high-entropy alloy, *Acta Mater.* 147 (2018) 236–246.
- [23] S. Mahajan, C.S. Pande, M.A. Imam, B.B. Rath, Formation of annealing twins in F.C.C. crystals, *Acta Mater.* 45 (1997) 2633–2638.
- [24] T. Guo, J. Li, J. Wang, W.Y. Wang, Y. Liu, X. Luo, H. Kou, E. Beaugnon, Microstructure and properties of bulk Al<sub>0.5</sub>CoCrFeNi high-entropy alloy by cold rolling and subsequent annealing, *Mater. Sci. Eng. A* 729 (2018) 141–148.
- [25] C. Haase, L. Mora, Influence of deformation and annealing twinning on the microstructure and texture evolution of face-centered cubic high entropy alloys, *Acta Mater.* 150 (2018) 88–103.
- [26] S. Papula, S. Anttila, J. Talonen, T. Sarikka, I. Virkkunen, Strain hardening of cold-rolled lean-alloyed metastable ferritic-austenitic stainless steels, *Mater. Sci. Eng. A* 677 (2016) 11–19.
- [27] D.T. Pierce, J.A. Jimenez, J. Bentley, D. Raabe, J.E. Wittig, The influence of stacking fault energy on the microstructural and strain-hardening evolution of Fe–Mn–Al–Si steels during tensile deformation, *Acta Mater.* 100 (2015) 178–190.
- [28] M. Calcagnotto, D. Ponge, E. Demir, D. Raabe, Orientation gradients and geometrically necessary dislocations in ultrafine grained dual-phase steels studied by 2D and 3D EBSD, *Mater. Sci. Eng. A* 527 (2010) 2738–2746.
- [29] M. Frank, S.S. Nene, K. Liu, R.S. Mishra, R.E. Brennan, K. Cho, Z. Li, D. Raabe, Dynamic phase stabilization and resultant mechanical properties upon friction stir processing of a metastable interstitial high entropy alloy, Manuscript under preparation (2018).
- [30] J. Shi, X. Sun, M. Wang, W. Hui, H. Dong, W. Cao, Enhanced work-hardening behavior and mechanical properties in ultrafine-grained steels with large-fractioned metastable austenite, *Scripta Mater.* 63 (2010) 815–818.
- [31] C. Herrera, D. Ponge, D. Raabe, Design of a novel Mn-based 1 GPa duplex stainless TRIP steel with 60% ductility by a reduction of austenite stability, *Acta Mater.* 59 (2011) 4653–4664.
- [32] P.J. Jacques, E. Girault, P. Harlet, F. Delannay, The developments of cold-rolled trip-assisted multiphase steels, low silicon trip-assisted multiphase steels, *ISIJ Int.* 41 (2001) 1061–1067.
- [33] G. Frommeyer, U. Brüx, P. Neumann, Supra-ductile and high-strength manganese-trip/twip steels for high energy absorption purposes, *ISIJ Int.* 43 (2003) 438–446.